\$ STORY OF THE STO

Contents lists available at ScienceDirect

Earth and Planetary Science Letters

www.elsevier.com/locate/epsl



Pushing the limits: Resolving paleoseawater signatures in nanoscale fluid inclusions by atom probe tomography



S.D. Taylor a,*, D.D. Gregory b, D.E. Perea c, L. Kovarik J.B. Cliff C, T.W. Lyons d,**

- ^a Physical and Computational Sciences Directorate, Pacific Northwest National Laboratory, Richland, WA 99354, USA
- ^b Department of Earth Sciences, University of Toronto, Toronto, ON M5S 3B1, Canada
- ^c Earth and Biological Sciences Directorate, Pacific Northwest National Laboratory, Richland, WA 99354, USA
- ^d Department of Earth and Planetary Sciences, University of California, Riverside, CA 92521, USA

ARTICLE INFO

Article history: Received 13 June 2022 Received in revised form 28 September 2022 Accepted 1 October 2022 Available online 12 October 2022

Keywords: fluid inclusion pyrite seawater chemistry atom probe tomography

Editor: A. Jacobson

ABSTRACT

New insight into the geochemistry of ancient environments can be gained through structural and chemical analyses of nanometer-scale features within minerals. Here, we present recent developments using atom probe tomography (APT) enabling direct visualization of nanoscale fluid inclusions trapped within pyrite (FeS₂) and thereby chemical characterization of remnant seawater. Pyrite framboids (spherical clusters of nanocrystals) were sampled from the Middle Devonian Leicester Pyrite Member (New York). Scanning transmission electron microscopy shows low density features distributed within the pyrite (<4 nm in size). Three-dimensional chemical visualization and analysis by APT reveals these to be nanoscale fluid inclusions preserving the elemental signatures of the water column in which the framboids formed, as alkalis consistent with seawater including Na, K, Mg, and Ca are identified. Further, within the inclusions Mg/Ca is measured to be \sim 0.6 \pm 0.2 – consistent with conditions for calcitedominated seawater existing in the Middle Devonian. The results and approach developed in this study show the potential to reconstruct paleoenvironmental conditions from coupled elemental and structural analyses of nanoscale fluid inclusions.

© 2022 Elsevier B.V. All rights reserved.

1. Introduction

Reconstructing Earth's environmental conditions in the geologic past can be achieved through analysis of fluid inclusions trapped during growth of minerals at or near Earth's surface (Goldstein, 2001; Lowenstein et al., 2001). For instance, the chemistry of fluid inclusions within halite from marine deposits can track secular changes in seawater chemistry, including oscillations across time (Balthasar and Cusack, 2015). Despite many past successes, the full wealth of information about paleoenvironmental conditions possible from analysis of fluid inclusions remains largely untapped given the constraints on material systems, inclusions size, and techniques available for inclusion analysis. Transparent minerals like halite (NaCl) and calcite (CaCO₃) have historically been emphasized, as inclusions are observable using optical techniques (Brennan and Lowenstein, 2002), although this approach limits coverage

of the stratigraphic record. Further, characterization is often limited to at least micrometer-sized inclusions as required by conventional techniques, such as laser ablation inductively coupled mass spectrometry (LA-ICP-MS) and scanning electron microscopy energy dispersive spectroscopy (SEM-EDS) (Johnson and Goldstein, 1993; Lowenstein et al., 2001). While nanometer-scale (referred to as nanoscale here) fluid inclusions are prevalent (Bodnar and Samson, 2003), the capacity in which paleoenvironmental conditions can be inferred is largely overlooked given the limited knowledge and techniques available for such efforts.

In this study we seek to overcome these long-standing barriers, presenting new capabilities and insight into fluid inclusion analysis at the atomic level. High-resolution microscopy techniques such as scanning transmission electron microscopy (STEM) can identify inclusions as microstructural defects, although compositional analyses are limited due to projection issues (i.e., characterization of three-dimensional (3D) features is based on two-dimensional (2D) renderings) and its low chemical-sensitivity (e.g., inability to resolve light elements like H) (Viti and Frezzotti, 2001; Deditius et al., 2009; Parish et al., 2015). Conversely, atom probe tomography (APT) is a recognized and powerful analytical technique for the chemical characterization of clusters/precipitates within solids in 3D with sub-nanometer-scale, barring fine-scale aberrations due

^{*} Corresponding author at: Physical Sciences Division, Pacific Northwest National Laboratory, Richland, WA 99354, USA.

^{**} Corresponding author at: Department of Earth Sciences, University of California, Riverside, CA 92521, USA.

 $[\]hbox{\it E-mail addresses: } sandra.taylor@pnnl.gov (S.D. Taylor), timothy.lyons@ucr.edu (T.W. Lyons).$

ion trajectory overlaps and local magnification effects (Marquis and Vurpillot, 2008; Marquis and Hyde, 2010; Gault et al., 2021) (refs therein). The recent advent in the analyses of nanoscale defects and their interpretation enabled by these techniques have provided unprecedented insight into geologic processes, from crystal growth/recrystallization mechanisms (Fougerouse et al., 2016; Taylor et al., 2018, 2019) to interpreting geochronologic events (Moser et al., 2013; Valley et al., 2014; Peterman et al., 2016; White et al., 2017). The utility of APT in resolving inclusions has only been recently demonstrated in minerals, such as pyrite (FeS₂) (Dubosq et al., 2020; Reddy et al., 2020; Daly et al., 2021; Dubosq et al., 2021; Liu et al., 2022), although deep insight into the chemistry and paleoenvironmental significance of these features has not been achieved.

Here, we build on these analytical advances to directly visualize and characterize nanoscale water-filled inclusions within pyrite. Identification and microstructural characterization of the inclusions was achieved by STEM while APT was used to measure the chemical composition within the inclusions, with the goal of tracking paleo-seawater chemistry. We chose a framboidal pyrite specimen from the Devonian period with a well-known geologic history for context (Formolo and Lyons, 2007). In general, chemical signatures within the nanoscale fluid inclusions and compositional analyses, such as Mg/Ca ratios, are consistent with previous studies (Horita et al., 2002; Demicco et al., 2005). This study provides new insight into nanoscale fluid inclusion analyses that may enable exploration of paleoenvironmental conditions across a broad range of environments and timescales. Additionally, our analyses using pyrite present the potential to expand Mg/Ca measurements from evaporitic environments to major sedimentary minerals, thereby further improving ancient records for seawater chemistry.

2. Material and methods

2.1. Specimen information

Pyrite framboids were sampled from the Leicester Pyrite Member (LPM) in the Devonian Appalachian Basin (New York, *ca.* 390 Ma) (Baird and Brett, 1986). The LPM is a sedimentary lag deposit that crops out over hundreds of kms in upstate New York, comprised of a complex mixture of early- and later-formed pyrite reworked from the overlying strata—along with pyrite formed at the same time as formation of the LPM (Formolo and Lyons, 2007). The latter would reflect dominantly low but dynamic oxygen conditions in the bottom waters, including the likelihood of intermittent euxinia (Sageman and Lyons, 2003; Formolo and Lyons, 2007).

Samples were collected from the outcrop at Fall Brook of the LPM (42°53′60″N, 78°29′32″W) (outcrop location provided in the Supplementary Information (SI), Fig. S1). To avoid surface oxidation, samples were taken tens of centimeters into the outcrop and those in the interior of the hand specimen were selected for analyses. Samples were mounted in epoxy and polished to a final of 1 μ m diameter.

2.2. Analytical protocols

A nodule containing several individual framboids was located using a combination of reflected light microscopy and SEM (Fig. S2a). The texture of the pyrite framboids was resolved by chemical-imaging by nanoscale secondary ion mass spectrometry (NanoSIMS), using a CAMECA NanoSIMS 50L. Prior to analysis, samples were coated with 10 nm of high purity Ir to improve conductivity. All images reported here were collected as two frames consisting of 256×256 pixels collected with a dwell time of 13.5 ms pixel⁻¹. NMR magnetic field regulation was employed in all cases. Negative secondary ion images were collected using a

16 keV Cs⁺ primary ion beam. Secondary ions were accelerated to 8 keV and were collected using electron multipliers. Prior to image analysis, image areas were pre-sputtered with about 2×10^{16} ions cm⁻² Cs⁺. Ion images of $^{12}\text{C}_2^-$ and $^{34}\text{S}^-$ were collected using a 2pA primary beam that had a diameter of approximately 120 nm. Analysis of the images was performed using OpenMIMS and ImageJ (Abramoff et al., 2004). Consecutive frames were deadtime corrected on a pixel \times pixel basis, aligned, and summed.

Select framboids of interest were analyzed by APT and/or STEM based on their paragenesis, as described below. Specimens were prepared using a dual-beam SEM (Thermo Fisher Scientific Helios Nanolab 600i) using conventional focused ion beam (FIB) capabilities (Giannuzzi and Stevie, 1999; Thompson et al., 2007) (see SI for further details, Fig. S1) and mounted onto Si half- grids (Dune Sciences, OR, USA).

TEM was performed with an aberration-corrected FEI Titan 80-300 operated at 300 kV to characterize the pyrite and inclusion microstructure. The microscope incorporates a CEOS GmbH double-hexapole aberration corrector for the probe-forming lens, which allows imaging with $\sim\!0.8$ nm resolution in STEM mode. The presented images were acquired in STEM mode using a high-angle annular dark-field detector with beam convergence of 17.8 mrad and collection angle of 54 mrad. All images were acquired with TIA software package.

APT specimens were analyzed in a CAMECA Local Electrode Atom Probe (LEAP 4000 X-HR) at a set-point temperature of 40 K, a laser pulse repetition rate of 125 kHz, and a detection rate of 0.004-0.005 ions per pulse (maintained by varying the applied specimen voltage). The laser wavelength was 355 nm, and laser energy per pulse was 40 pJ. The data were reconstructed using the Integrated Visualization and Analysis Software (IVAS 3.8.5) developed by CAMECA. An average atomic volume of 0.013 nm³ atom $^{-1}$ was specified in the 3D reconstruction, representing the atomic density in the pyrite lattice (i.e., ~ 75 atoms nm $^{-3}$). Reconstructions were based on images and measurements of the tip profile, adjusting the image compression factor to better match tip radii. A voxel size of 1.0 \times 1.0 \times 1.0 nm and delocalization of 3.0 \times 3.0 \times 3.0 nm was applied.

A detailed description of the APT analytical procedure is provided in the SI, to which the reader is referred to for more detail. In brief, the specimen chemistry was reconstructed by assigning ionic species to each mass-to-charge state peak in the generated spectra to best reproduce the expected elemental and isotopic compositions. Elemental compositions and ratios were calculated relative to the ion counts detected within the measured volume. Analyses were conducted on a museum-grade pyrite specimen as a standard sample (see SI), providing reliable elemental measurements on the LPM. A total of four APT specimens from a single framboid in the LPM were analyzed by both STEM and APT, all of which observed similar general structural and chemical features at the nanoscale. One specimen is described in detail in the main text as a representative sample.

To identify fluid inclusions, ion segregation/clustering was probed via various APT techniques. Elemental distributions were visualized to gain firsthand observations for clustering. To quantitatively confirm and describe the extent to which ions segregate and cluster, statistical analyses and random comparator techniques were conducted (see SI for additional details) (Stephenson et al., 2007; Perea et al., 2015; Taylor et al., 2018). In brief, using nearest neighbor (NN) analyses, the distances between designated solute ions in the experimental specimen were measured and compared to that for a simulated dataset where ions are randomly distributed. The tendency for an ion to cluster was determined by quantifying the deviation in the NN distributions between the experimental and simulated datasets based on the Pearson coefficient μ (calculation in SI), where if $\mu=0$ the solute distribution is com-

pletely random while if $\mu=1$ the distribution is non-random and the ions are spatially associated, consistent with that expected for inclusions. Point density variations were also observed using 2D heat maps to confirm the identified clusters were consistent with previous APT descriptions for fluid inclusions (Dubosq et al., 2020).

3. Results and discussion

3.1. Identification of nanoscale fluid inclusions

3.1.1. Pyrite framboid paragenesis

For this study, it was of particular interest to probe pyrite framboids that formed in the water column, as we postulate these are more likely to archive seawater compositions at their time of formation-in contrast to diagenetic pyrite which forms in the sediments within pore waters that may be shifted dramatically in composition from the overlying waters. Some of the pyrite from the LPM was previously deduced to be water-column derived from analyses using Mo as a proxy for formation conditions (Gregory, 2020). In brief, using LA-ICP-MS, Mo concentrations measured within small pyrite framboids (<10 um) ranged from 80 to 400 ppm. Both the small sizes and Mo enrichments are consistent with environments reflecting euxinic deposition (Gregory et al., 2022). The Mo contents of the LPM samples were also at least an order of magnitude higher than those of framboids deposited under modern oxic water columns (median values range from 5-40 ppm) (Gregory et al., 2014); see Formolo and Lyons (2007) for additional evidence of euxinic deposition. Thus, it is expected that some material from the LPM can preserve seawater conditions from the initial formation time.

A nodule containing several individual framboids was imaged by NanoSIMS to resolve the framboid texture more clearly and further infer its formation conditions (Fig. 1a). The framboids were generally shown to be <10 µm in diameter and to consist of clusters of microscopic pyrite crystals. The presence of these smaller framboids suggests their likely formation in the sulfidic (euxinic) water column (Wilkin et al., 1996). The framboidal texture is also indicative of pyrite formation at a high degree of supersaturation (Rickard, 2012) that usually forms very early, either in the water column or during sedimentation (Rickard, 2019, 2021; Wilkin et al., 1996). Pyrite formed later in sedimentation due to diffusional overprint is usually coarser grained (Gregory et al., 2022). Metamorphic recrystallization is also coarser grained and non-framboidal (Large et al., 2011, 2009).

3.1.2. Microstructural and chemical characterization

Framboids on the outer edge of the nodule with the specified characteristics were targeted for microstructural characterization using STEM (Fig. 1a). High-resolution imaging highlights the assemblage of numerous sub-micrometer scale crystals (~400 nm in diameter) with well-formed (euhedral) crystal faces forming framboids, bound together with a nano-porous pyrite cement (Fig. 1b). Furthermore, nanoscale low-density features are found to be littered within the primary pyrite grain; the features are typically <4 nm in size and are mostly spherical in shape (a fraction also appears ellipsoidal). The features are densely packed with a spacing typically <2 nm, although the actual distance can deviate given the nature of the image as a 2D projection; this was also evaluated by 3D APT (discussed shortly).

APT specimens were prepared from a nearby framboid with similar characteristics (Fig. 1b, Fig. S2), and analyzed by both STEM and APT to directly correlate structural and chemical features at the nanoscale, respectively. STEM imaging of a tip shows the nanoscale, low-density features scattered within crystalline pyrite (Fig. 2a), consistent with the nanotexture observed in primary grains, i.e., the features were mostly spherical in morphology

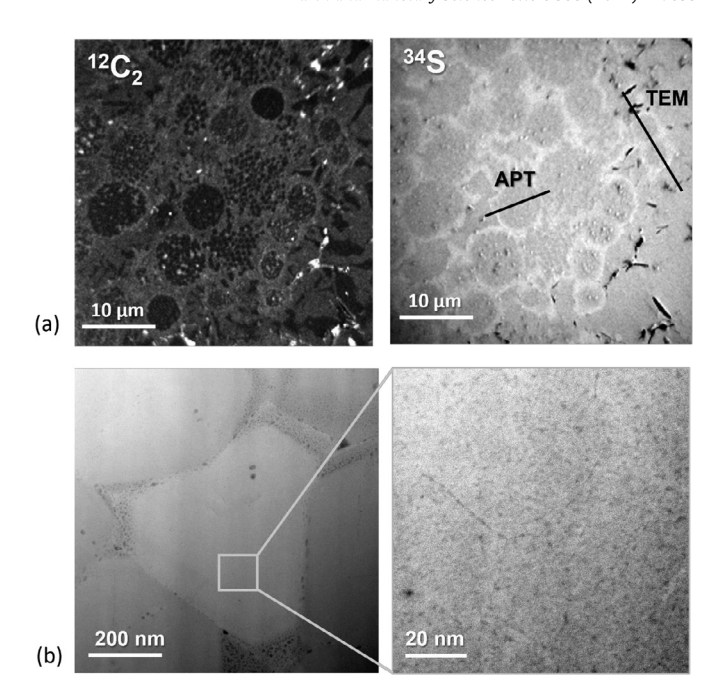


Fig. 1. Diagnostic features for the Leicester pyrite member. (a) Chemical mapping with NanoSIMS using $^{12}C_2$ and ^{34}S species, denoting the framboids specifically probed by STEM and APT. (b) STEM imaging of framboids (marked as TEM in panel "a") consisting of euhedral pyrite nanoparticles within a porous, disordered pyrite matrix. Low-density regions exist at the nanoscale in the crystalline pyrite bulk.

with an average diameter of \sim 3 nm and appear densely packed. APT compositional analyses indicates that the chemistry is consistent with that expected for pyrite (e.g., the samples averaged \sim 35 atomic % (at.%) Fe and \sim 61 at.% S compared to 33at.% and 67at.% for stoichiometric pyrite, respectively). Visualization of the distribution of Fe and S ions shows they are homogeneously distributed in the specimen, indicating the major element chemistry of the pyrite matrix is consistent across the specimen (Fig. 2b).

Interestingly, several impurities including hydrated species, alkalis (i.e., Na, Mg, K, and Ca), and nonmetal species (i.e., organics as well as Se and Br) are present (Fig. 3a, b). Identification was aided through analysis of a pyrite standard (see SI for more details, Fig. S2) and referring to previous APT characterizations of this mineral (Dubosq et al., 2019; Fougerouse et al., 2019, 2021; Gopon et al., 2019; Wu et al., 2019), and confirm these impurities are unique to the LPM specimens. The detection of hydrated ionic species in the form of hydroxide and iron-hydroxide ions is particularly interesting, as they suggest the presence of water in the specimen. That is, H_2O^{1+} and H_3O^{1+} species at 18-19 Da (collectively referred to as H_xO species) are readily measured and account for $\sim 0.7\%$ of all ionic species measured within the pyrite tips (averaged across the four APT specimens analyzed), while FeHO²⁺ and FeH₂O²⁺ species at 35.5-38Da (FeH $_{\rm x}$ O species) account for \sim 0.6% of all ionic species. While APT is a solid-phase characterization technique and cannot directly probe pure liquid states, the presence of related hydrated ionic-species can be used to infer the presence of aqueous components (Schreiber et al., 2018; El-Zoka et al., 2020; Liu et al., 2022). These signatures are similar to those observed in a hydrated fayalite, where APT analyses showed HxO and FeHxO species localized within nanoscale defects (Liu et al., 2022).

3.1.3. Cluster analysis

Identification and characterization of nanoscale fluid inclusions within the pyrite matrix by APT was enabled through various cluster analysis techniques. Given the clear presence of hydrated ionic species, the distribution of H_xO and FeH_xO ions were visualized in 3D to observe ion segregation/clustering that would be consistent

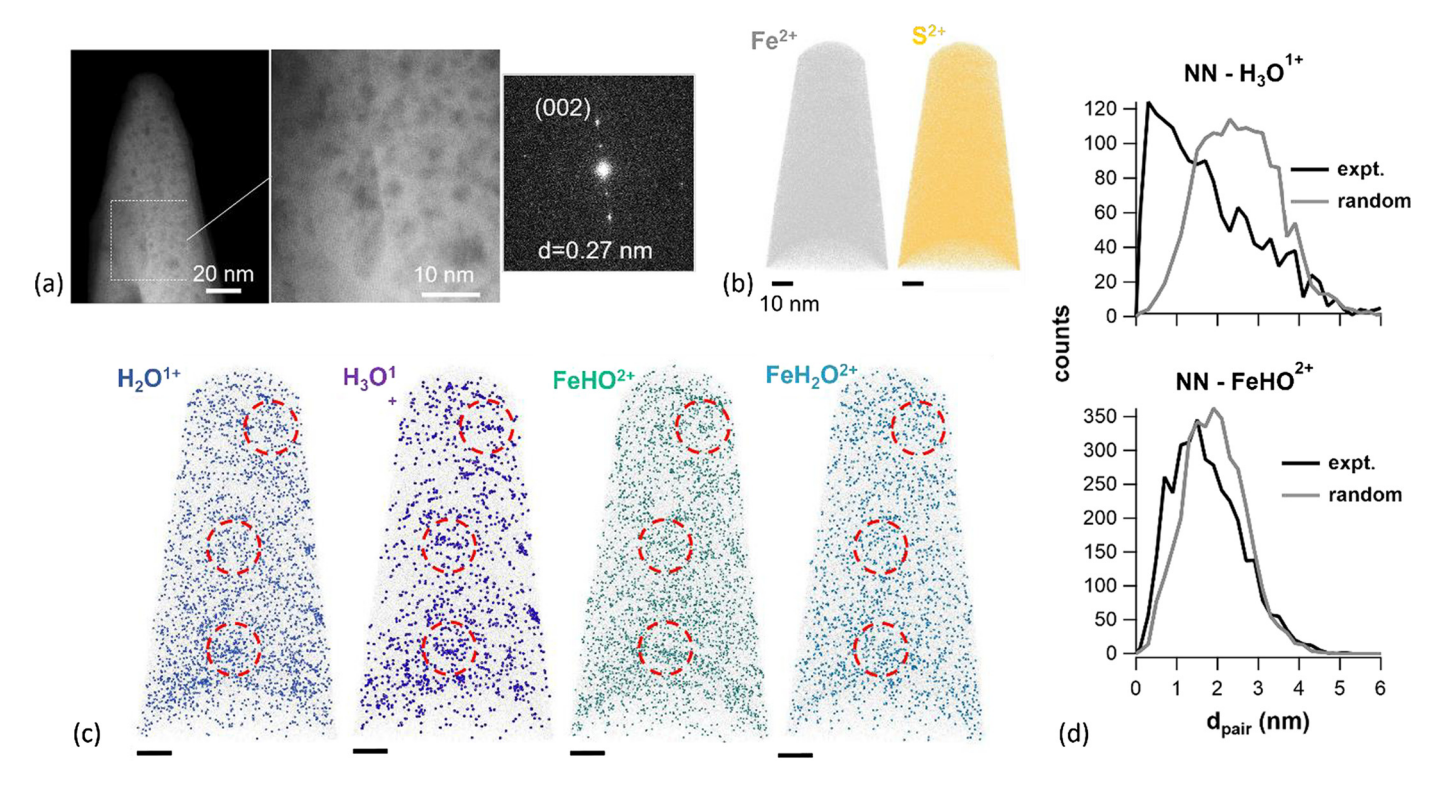


Fig. 2. Correlative STEM/APT analysis showing inclusions within pyrite from the LPM specimen. (a) STEM imaging of APT specimen showing the presence of low-density regions in pyrite. Correlative fast fourier transform analysis shows lattice diffraction spots corresponding to (002) planes in pyrite (lattice spacing of 0.27 nm), confirming the specimen crystallinity. APT atomic maps showing the distribution of (b) Fe^{2+} and Fe^{2+} ionic-species and (c) hydrated species H_2O^{1+} , H_3O^{1+} , $FeHO^{2+}$, and FeH_2O^{2+} . Red circles are used to correlate the distributions to specific regions. Ion sizes are exaggerated for clarity. (d) NN analyses for H_3O^{1+} compared to $FeHO^{2+}$. (For interpretation of the colors in the figure(s), the reader is referred to the web version of this article.)

with the nature of ions in fluid inclusions. In particular, H_x O-ions were readily observed as clusters within the pyrite matrix (Fig. 2c). FeH_xO-ions also appear to cluster to some extent although this was more ambiguous based on visual inspection alone.

To better inform observations for ion clustering/segregation and in turn identify species representative of inclusions, statistical analyses were conducted. For instance, NN analyses show H₃O¹⁺ ions are within spatial proximity to one another compared to the simulated dataset where ion distributions are randomized (i.e., the modes for the inter-ionic distances measured are 0.3 nm vs. 2.3 nm, respectively) (Fig. 2d). The deviation in the NN distributions between the experimental and simulated datasets is significant ($\mu = 0.9$) and confirms strong clustering, consistent with that expected for ions associated with inclusions. In comparison, NN analyses of shows FeHO¹⁺ also clusters but less strongly than H₃O¹⁺ (i.e., modes for the inter-ionic distances were 1.4 nm vs. 1.9 nm, respectively, with $\mu = 0.39$). Overall, statistical analyses across the four specimens consistently showed H_xO-species to strongly cluster (average μ for H_2O^{1+} and H_3O^{1+} are 0.7 and 0.9, respectively) compared to FeH_xO-ions (average μ for FeHO²⁺ and FeH_2O^{2+} are 0.5 and 0.3, respectively) (Fig. 2c, d; Table S1). In turn, these analyses complement direct observations of the elemental distributions and enable us to reliably deduce nanoscale fluid inclusions based on H_xO species.

Morphological/structural characterization of the inclusions by APT is qualitatively similar to that observed for the low-density features by STEM. That is, 3D visualization of $\rm H_xO$ clusters as isosurfaces shows the inclusions are typically ~ 1 –10 nm in diameter and the morphology is spherical to oblate (Fig. 4a). These observations are nominally consistent to that from STEM, although structural information at the sub-nanometer scale is limited due to inherent spatial aberrations and distortions resulting from the analysis of chemically complex nanostructures by APT (Vurpillot et

al., 2000; Marguis and Vurpillot, 2008; Devaraj et al., 2014; Perea et al., 2016; Dubosq et al., 2020). Each cluster consists of \sim 10 to \sim 200 H_xO-ions, with the number of clusters varying among the APT tips from \sim 60-100 (select clusters are shown in Fig. 4a for clarity). The clusters are typically densely-packed with spacings of \sim 2-5 nm, although less densely-packed regions are also present. The clusters are also shown to be consistent with fluid inclusions based on 2D ion density maps (Fig. 4b); i.e., the higher ion density in the inclusion compared to the matrix is due to the concave shape of the inclusion walls focusing ion evaporation paths and low-field constituents in the inclusions evaporating faster, as observed in previous APT studies (Dubosq et al., 2020). Thus, combined with the observations of nanoscale lowdensity features within the pyrite from correlative STEM imaging, this study presents strong evidence for nanoscale water-filled inclusions within pyrite.

3.2. Evaluation of seawater chemistry

In addition to water, several alkali and alkaline elements (i.e., Na, Mg, K, and Ca) were also observed (Fig. 3b). These ions were visualized across the APT tips and were found to largely exist in clusters, with subtle variations in their spatial distributions (Fig. 4b, c). For example, Na, K, and Ca strongly cluster, while Mg also clusters but not as strongly (further supported by statistical analyses in Table S1; average $\mu=0.9,\,0.7,\,0.7,\,$ and 0.5, respectively). The ions also appear largely associated with the fluid inclusions. That is, compositional measurements within the HxO-cluster volumes show that the alkalis are more concentrated within the inclusions compared to the matrix (Fig. 4d), e.g., Na decreases an order of magnitude from >0.3 at.% in the inclusion to ~0.05 at.% in the matrix while Mg shows a more subtle decrease from ~0.02 at.% to ~0.01 at.%.

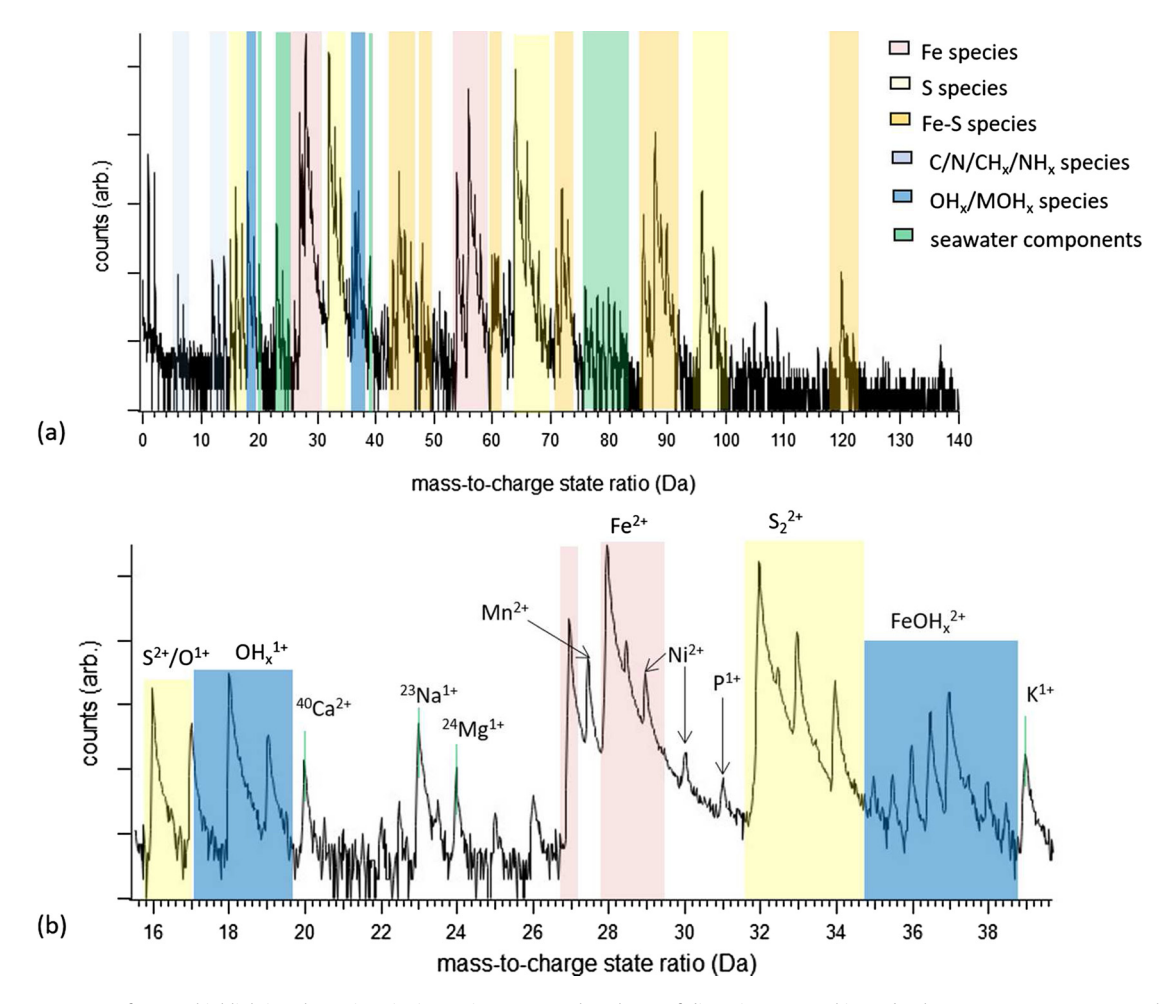


Fig. 3. (a) APT mass spectra for LPM highlighting the various ionic species present. Though not of direct interest to this study, the seawater components at the 76–82 Da are Se and Br. (b) Mass peaks highlighting hydrated and major alkali ionic species of interest to this study. Counts are shown on a logarithmic scale.

Table 1Alkali compositional measurements from the inclusions across the four APT specimens. Specimen 3 is the representative specimen shown in Figs. 2–4. Measurements are compared to those from previous studies including § Horita et al. (2002) and $^\ddag$ Demicco et al. (2005), For Demicco et al. (2005), a range of values for the elemental ratios are provided based on estimations from all four models tested. The error within individual specimens is represented by the uncertainty (2 σ ; 95% confidence interval) while the error in the average across the tips is represented by the standard deviation (25D).

		Predicted water-column chemistry		
		Mg/Ca	K/Ca	Na/Ca
		0.8-0.9, < 1.5§	\sim 0.3–0.8 ‡	$\sim \! 10 21^{\ddagger}$
		\sim 0.5–1.4 ‡		
		Measured inclusion chemistry ($\pm~2\sigma$)		
LPM	# atoms	Mg/Ca	K/Ca	Na/Ca
specimen	collected			
1	1.76×10^{6}	0.52 ± 0.13	1.52 ± 0.29	3.53 ± 0.60
2	2.25×10^{6}	0.87 ± 0.20	1.87 ± 0.34	4.15 ± 0.70
3	3.96×10^{6}	0.52 ± 0.10	1.60 ± 0.24	3.25 ± 0.43
4	1.38×10^{6}	0.50 ± 0.17	1.77 ± 0.43	5.67 ± 1.18
Average composition (\pm 2SD)		0.60 ± 0.15	1.69 ± 0.14	4.15 ± 0.94

The alkalis detected are consistent with major cations found in seawater and thus suggest that remnants of (paleo)seawater may have been entrained within the pyrite during growth. In an effort to assess whether the elemental signature of the water column in which the framboids formed is captured and preserved, we quantified the alkali ion concentrations associated with the fluid inclusions in our sample and compared this to previously predicted compositions for seawater in the Devonian, based on measurements from halite inclusions (Horita et al., 2002) as well as models (Demicco et al., 2005). Concentrations are expressed as ratios relative to Ca.

Mg/Ca measurements from the inclusions in the LPM specimen (averaging 0.6 ± 0.2 across the four APT specimens) are in reasonable agreement with that predicted for the Middle Devonian (i.e., ~0.8 –0.9, with a maximum of 1.5, based on direct measurement of inclusions by Horita et al. (2002) or within ~0.5 –1.4, based on models by Demicco et al. (2005)) (Table 1). Measurements across the four specimens were generally consistent and within error of one another.

Although measurements of K and Na concentrations are not well-established for the Devonian and are poorly constrained across geologic time in general, we probed their concentrations

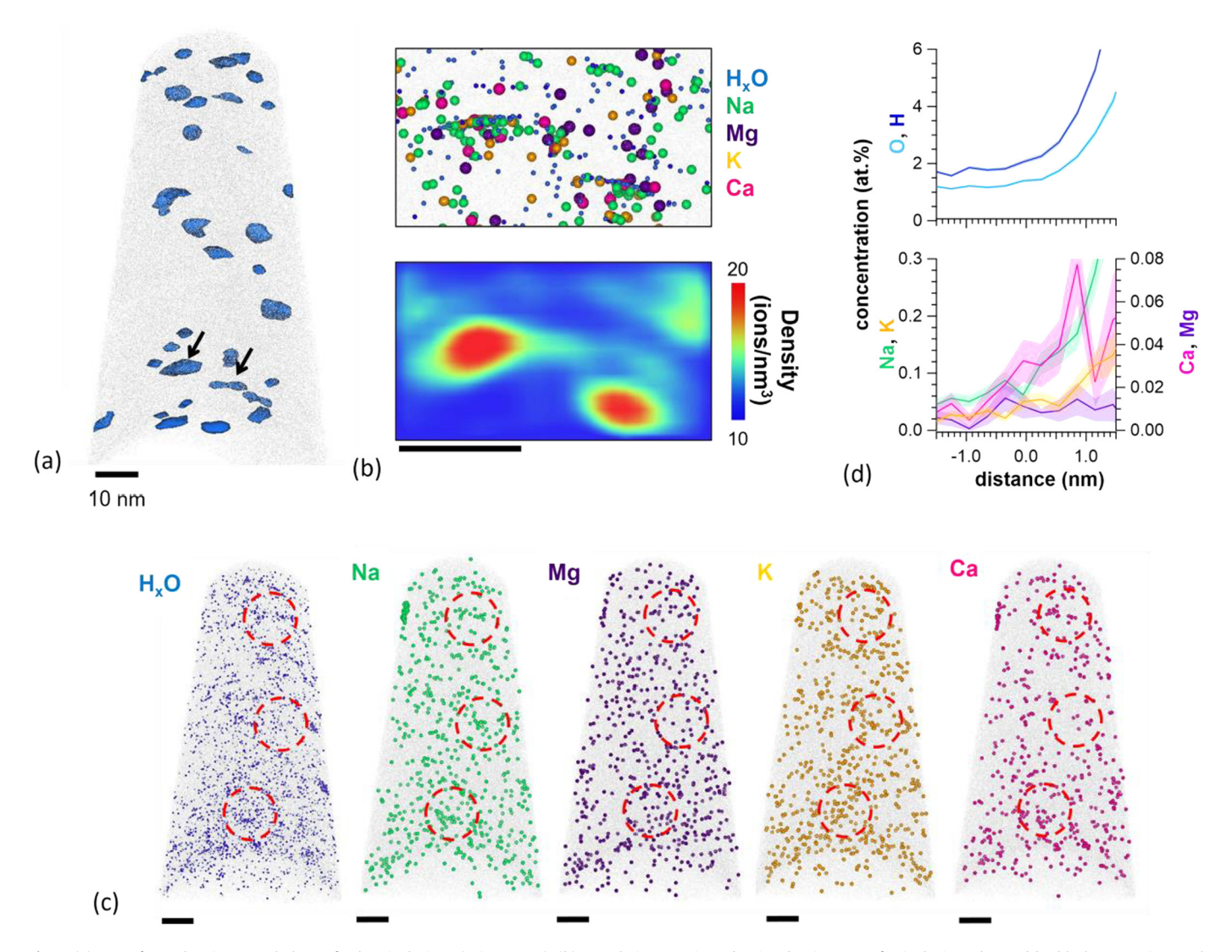


Fig. 4. (a) Isosurfaces showing morphology of select inclusions (2 ion% H_xO). (b) Correlative atomic and point density maps for inclusions denoted by black arrows in panel (a). (c) Atomic maps visualizing the distribution of H_xO , Na, Mg, K, and Ca species across the specimen. Ion sizes are exaggerated for clarity. Gray atoms represent Fe in the pyrite matrix. Red circles are used to correlate the distribution to specific regions. (d) Volumetric compositional analysis within H_xO -isosurfaces showing the elemental distribution of alkalis in inclusions (positive distances) relative to the matrix (negative distances). Error is represented by the shaded error bands (1σ , see SI for calculation); note, the error for O and H is more subtle due to the larger measurement scale.

within the inclusions as a secondary check. In contrast to Mg, measurements for K and Na from the LPM deviate from those predicted in previous studies by modeling. That is, K is overestimated with respect to modeled values during the Devonian (Demicco et al., 2005) (average K/Ca for LPM 1.7 \pm 0.1 vs. \sim 0.3-0.8, respectively) while Na is instead underestimated (i.e. 4.2 ± 0.9 vs. \sim 10-21, respectively).

While the ratios of Na and K deviate quantitatively from predicted values, we speculate the qualitative trends for Na and K may correlate to the expected brine composition and marine evaporite for the period. That is, Mg/Ca measurements here are consistent with that predicted for the Middle Devonian where paleoseawater is depleted in Mg and elevated in Ca, especially relative to present-day seawater compositions (i.e., Mg/Ca = 5.2) (Hardie, 1996; Lowenstein et al., 2001). At low Mg/Ca (i.e., < 2.0), calcite is the dominant non-skeletal carbonate while KCl is the dominant evaporite (whereas aragonite and MgSO₄ are dominant when Mg/Ca > 2.0, as in present-day conditions), loosely correlating to the higher K concentrations measured here. Similarly, the lower Na concentrations here may correlate to analyses of paleoseawaters with low Mg/Ca (e.g., from the Cambrian, Silurian, and Cretaceous) where Na was relatively depleted during halite precipitation

compared to that at high Mg/Ca, like present-day halite-saturated seawater brines.

The alkali composition in the bulk (i.e., the entire specimen including the matrix and inclusions) was compared to assess whether potential mass transfer reactions could have influenced compositional analyses of the inclusions. In general, alkali compositions are nominally consistent between the inclusions and the bulk, i.e., average Mg-, K-, and Na/Ca in the bulk are 0.9 ± 0.3 , 1.6 ± 0.2 , and 3.4 ± 0.6 (see SI, Table S2), within error of that measured in the inclusions (Table 1). It is possible processes like incorporation and/or diffusion occur, e.g., higher Mg/Ca in the bulk indicates a fraction of Mg is associated within the pyrite matrix in addition to the inclusions (consistent with our statistical analyses as well, Table S1). However, it is uncertain whether this would arise from diffusion between inclusions and the matrix or if ions are incorporated in the pyrite lattice during crystallization, as knowledge of these phenomena for alkali ions in pyrite is lacking; controlled and systematic experiments combined with modeling (beyond the scope of this paper) would provide valuable insight into these behaviors (Cherniak, 2010; Evans et al., 2020; Mavromatis et al., 2022). Overall, the comparable compositions between the inclusions and bulk indicate mass transfer between the inclusion with the matrix is not significant. Further, measurements for Mg/Ca within the inclusions are in reasonable agreement with that predicted to the Devonian (Horita et al., 2002; Demicco et al., 2005) and suggest paleoseawater signatures are effectively preserved.

4. Conclusions

This study presents new insight into the microstructural and chemical characterization of nanoscale fluid inclusions as well as their potential to explore paleoenvironmental conditions, enabled through correlative analyses using high-resolution techniques. Specifically, analyses were conducted on pyrite framboids from the middle-Devonian LPM formation with textures indicative of early-stage formation in a sulfidic (euxinic) water column, based on NanoSIMS characterization. Correlative STEM and APT analyses revealed the presence of nanoscale water-filled inclusions, as low-density features (typically <4 nm) homogeneously scattered within the pyrite matrix and distinct clusters of hydrated ionic-species were directly observed. Further, unique chemical signatures consistent with water-column chemistry were readily detected and included major ions from seawater (i.e., Na, Mg, K, and Ca). Quantification of the alkali concentrations indicate that the fluid inclusions contain marine salinities consistent with those hypothesized for the Middle Devonian, particularly Mg/Ca measurements (Demicco et al., 2005). These combined observations provide strong evidence that these pyrite regions are petrographically primary and have not undergone significant recrystallization or infiltration of diagenetic or metamorphic fluids.

The potential to resolve paleoseawater signatures and compositions through analyses of nanoscale features offers exciting opportunities. For example, this approach can be applied to access more thorough records of Mg/Ca to aid in tracking the occurrence of calcite versus aragonite seas across geologic time. Oscillations in the dominance of aragonite versus calcite in abiotic marine CaCO₃ precipitates throughout Earth history are closely coupled to the evolution of seawater composition more broadly and provide the environmental context for biomineralization of calcareous organisms (Folk and Land, 1975; Hardie, 1996; Lowenstein et al., 2001). CaCO₃ polymorph formation is linked to distinct Mg/Ca and temperature-dependent thresholds, with calcite forming at low temperatures and relatively low Mg/Ca (< 2.0), while aragonite forms at warm temperatures under higher Mg/Ca (> 2.0). Our measured Mg/Ca within the LPM specimen averaged 0.6 ± 0.2 , consistent with predictions of calcite seas dominating the Middle Devonian and independent estimates of Mg/Ca (\sim 0.8-0.9) (Lowenstein et al., 2001; Horita et al., 2002). The great abundance of pyritic euxinic shales through time elevates the temporal utility of the approach.

Continued technical development in the analyses of nanoscale fluid inclusions is needed, including evaluation of the chemical/structural nature of these features across a broader range of specimens of pyrite and within different minerals. It would be of particular interest to probe the chemistry of early-formed, pervasive-growth pyrite nodules relative to later-formed pyrite nodules reflecting concentric-growth mechanisms; these may provide a window into the chemistry of ancient ocean bottom waters where the latter may track the evolution of pore waters that have become partly or completely isolated from seawater (Gregory et al., 2019). The approach developed here is also more broadly applicable; for example, analyses of pyrite ores could provide salinity estimates for ore-related fluids and thus constrain genetic models. In turn, the ability to probe and characterize nanoscale fluid inclusions can potentially provide unprecedented insight into ancient paleoenvironments and the chemical evolution of diverse subsurface fluids, even in samples with complicated histories of mineralization and alteration.

CRediT authorship contribution statement

SDT and DEP were involved in specimen preparation, APT analysis, and data interpretation. LK was involved in TEM analysis. JBC was involved in SIMS analysis. DDG and TWL were involved sample acquisition, characterization, study design, and data interpretation. SDT, DDG, and TWL were involved in manuscript preparation.

Declaration of competing interest

The authors declare that they have no known competing financial interests or personal relationships that could have appeared to influence the work reported in this paper.

Data availability

Data will be made available on request.

Acknowledgements

Sample preparation and LEAP 4000 XHR analyses were performed on a project award (doi.org/10.46936/sthm.proj.2017.49860/60006201) from the Environmental Molecular Sciences Laboratory, a DOE Office of Science User Facility sponsored by the Biological and Environmental Research program under Contract No. DE-AC05-76RL01830 and located at PNNL. We thank Jeffery Over and Stephanie Olson for help during sample of the Leicester pyrite member. We further acknowledge funding through an NSERC Discovery Grant #04843 funding to Gregory.

Appendix A. Supplementary material

Supplementary material related to this article can be found online at https://doi.org/10.1016/j.epsl.2022.117859.

References

Abramoff, M.D., Magalhaes, P.J., Ram, S.J., 2004. Image processing with ImageJ. Biophon. Intl. 11, 36–42.

Baird, G.C., Brett, C.E., 1986. Erosion on an anaerobic seafloor: significance of reworked pyrite deposits from the Devonian of New York state. Palaeogeogr. Palaeoclimatol. Palaeoecol. 57, 157–193.

Balthasar, U., Cusack, M., 2015. Aragonite-calcite seas—quantifying the gray area. Geology 43, 99–102.

Bodnar, R.J., Samson, I., 2003. Introduction to fluid inclusions. In: Fluid Inclusions: Analysis and Interpretation, pp. 1–8.

Brennan, S.T., Lowenstein, T.K., 2002. The major-ion composition of Silurian seawater. Geochim. Cosmochim. Acta 66, 2683–2700.

Cherniak, D.J., 2010. Diffusion in carbonates, fluorite, sulfide minerals, and diamond. Rev. Mineral. Geochem. 72, 871–897.

Daly, L., Lee, M.R., Hallis, L.J., Ishii, H.A., Bradley, J.P., Bland, P.A., Saxey, D.W., Fougerouse, D., Rickard, W.D.A., Forman, L.V., Timms, N.E., Jourdan, F., Reddy, S.M., Salge, T., Quadir, Z., Christou, E., Cox, M.A., Aguiar, J.A., Hattar, K., Monterrosa, A., Keller, L.P., Christoffersen, R., Dukes, C.A., Loeffler, M.J., Thompson, M.S., 2021. Solar wind contributions to Earth's oceans. Nat. Astron. 5, 1275–1285.

Deditius, A.P., Utsunomiya, S., Ewing, R.C., Kesler, S.E., 2009. Nanoscale "liquid" inclusions of As-Fe-S in arsenian pyrite. Am. Mineral. 94, 391–394.

Demicco, R.V., Lowenstein, T.K., Hardie, L.A., Spencer, R.J., 2005. Model of seawater composition for the Phanerozoic. Geology 33, 877–880.

Devaraj, A., Colby, R., Vurpillot, F., Thevuthasan, S., 2014. Understanding atom probe tomography of cxide-supported metal nanoparticles by correlation with atomic-resolution electron microscopy and field evaporation simulation. J. Phys. Chem. Lett. 5, 1361–1367.

Dubosq, R., Rogowitz, A., Schweinar, K., Gault, B., Schneider, D.A., 2019. A 2D and 3D nanostructural study of naturally deformed pyrite: assessing the links between trace element mobility and defect structures. Contrib. Mineral. Petrol. 174, 72.

Dubosq, R., Gault, B., Hatzoglou, C., Schweinar, K., Vurpillot, F., Rogowitz, A., Rantitsch, G., Schneider, D.A., 2020. Analysis of nanoscale fluid inclusions in geomaterials by atom probe tomography: experiments and numerical simulations. Ultramicroscopy 218, 113092.

- Dubosq, R., Rogowitz, A., Schneider, D.A., Schweinar, K., Gault, B., 2021. Fluid inclusion induced hardening: nanoscale evidence from naturally deformed pyrite. Contrib. Mineral. Petrol. 176, 15.
- El-Zoka, A.A., Kim, S.H., Deville, S., Newman, R.C., Stephenson, L.T., Gault, B., 2020. Enabling near-atomic-scale analysis of frozen water. Sci. Adv. 6.
- Evans, D., Gray, W.R., Rae, J.W.B., Greenop, R., Webb, P.B., Penkman, K., Kröger, R., Allison, N., 2020. Trace and major element incorporation into amorphous calcium carbonate (ACC) precipitated from seawater. Geochim. Cosmochim. Acta 290, 293–311.
- Folk, R.L., Land, L.S., 1975. Mg/Ca ratio and salinity: two controls over crystallization of dolomite. AAPG Bull. 59, 60–68.
- Formolo, M.J., Lyons, T.W., 2007. Accumulation and preservation of reworked marine pyrite beneath an oxygen-rich devonian atmosphere: constraints from sulfur isotopes and framboid textures. J. Sediment. Res. 77, 623–633.
- Fougerouse, D., Reddy, S.M., Saxey, D.W., Rickard, W.D.A., van Riessen, A., Mickleth-waite, S., 2016. Nanoscale gold clusters in arsenopyrite controlled by growth rate not concentration: evidence from atom probe microscopy. Am. Mineral. 101, 1916–1919.
- Fougerouse, D., Reddy, S.M., Kirkland, C.L., Saxey, D.W., Rickard, W.D., Hough, R.M., 2019. Time-resolved, defect-hosted, trace element mobility in deformed Witwatersrand pyrite. Geosci. Front. 10, 55–63.
- Fougerouse, D., Reddy, S.M., Aylmore, M., Yang, L., Guagliardo, P., Saxey, D.W., Rickard, W.D.A., Timms, N., 2021. A new kind of invisible gold in pyrite hosted in deformation-related dislocations. Geology 49, 1225–1229.
- Gault, B., Chiaramonti, A., Cojocaru-Mirédin, O., Stender, P., Dubosq, R., Freysoldt, C., Makineni, S.K., Li, T., Moody, M., Cairney, J.M., 2021. Atom probe tomography. Nat. Rev. Methods Primers 1, 51.
- Giannuzzi, L.A., Stevie, F.A., 1999. A review of focused ion beam milling techniques for TEM specimen preparation. Micron 30, 197–204.
- Goldstein, R.H., 2001. Clues from fluid inclusions. Science 294, 1009-1011.
- Gopon, P., Douglas, J.O., Auger, M.A., Hansen, L., Wade, J., Cline, J.S., Robb, L.J., Moody, M.P., 2019. A nanoscale investigation of Carlin-type gold deposits: an atom-scale elemental and isotopic perspective. Econ. Geol. 114, 1123–1133.
- Gregory, D.D., 2020. The Pyrite Trace Element Paleo-Ocean Chemistry Proxy. Cambridge University Press, Cambridge.
- Gregory, D., Meffre, S., Large, R., 2014. Comparison of metal enrichment in pyrite framboids from a metal-enriched and metal-poor estuary. Am. Mineral. 99, 633–644.
- Gregory, D., Mukherjee, I., Olson, S.L., Large, R.R., Danyushevsky, L.V., Stepanov, A.S., Avila, J.N., Cliff, J., Ireland, T.R., Raiswell, R., Olin, P.H., Maslennikov, V.V., Lyons, T.W., 2019. The formation mechanisms of sedimentary pyrite nodules determined by trace element and sulfur isotope microanalysis. Geochim. Cosmochim. Acta 259, 53–68.
- Gregory, D.D., Lyons, T.W., Large, R.R., Stepanov, A.S., 2022. Ground-truthing the pyrite trace element proxy in modern euxinic settings. Am. Mineral. 107, 848–859.
- Hardie, L.A., 1996. Secular variation in seawater chemistry: an explanation for the coupled secular variation in the mineralogies of marine limestones and potash evaporites over the past 600My. Geology 24, 279–283.
- Horita, J., Zimmermann, H., Holland, H.D., 2002. Chemical evolution of seawater during the Phanerozoic: implications from the record of marine evaporites. Geochim. Cosmochim. Acta 66, 3733–3756.
- Johnson, W.J., Goldstein, R.H., 1993. Cambrian seawater preserved as inclusions in marine low-magnesium calcite cement. Nature 362, 335–337.
- Large, R.R., Bull, S.W., Maslennikov, V.V., 2011. A carbonaceous sedimentary sourcerock model for Carlin-type and orogenic gold deposits. Econ. Geol. 106 (3), 231, 358
- Large, R.R., Danyushevsky, L., Hollit, C., Maslennikov, V., Meffre, S., Gilbert, S., Bull, S., Scott, R., Emsbo, P., Thomas, H., Singh, B., Foster, J., 2009. Gold and trace element zonation in pyrite using a laser imaging technique: implications for the timing of gold in orogenic and carlin-style sediment-hosted deposits. Econ. Geol. 104 (5) 635–668.
- Liu, J., Taylor, S.D., Qafoku, O., Arey, B.W., Colby, R., Eaton, A., Bartrand, J., Shutthanandan, V., Manandhar, S., Perea, D.E., 2022. Visualizing the distribution of water in nominally anhydrous minerals at the atomic scale: insights from atom probe tomography on fayalite. Geophys. Res. Lett. 49.
- Lowenstein, T.K., Timofeeff, M.N., Brennan, S.T., Hardie, L.A., Demicco, R.V., 2001. Oscillations in Phanerozoic seawater chemistry: evidence from fluid inclusions. Science 294, 1086–1088.

- Marquis, E.A., Hyde, J.M., 2010. Applications of atom-probe tomography to the characterisation of solute behaviours. Mater. Sci. Eng. Rep. 69, 37–62.
- Marquis, E.A., Vurpillot, F., 2008. Chromatic aberrations in the field evaporation behavior of small precipitates. Microsc. Microanal. 14, 561–570.
- Mavromatis, V., Brazier, J.-M., Goetschl, K.E., 2022. Controls of temperature and mineral growth rate on Mg incorporation in aragonite. Geochim. Cosmochim. Acta 317, 53–64.
- Moser, D.E., Chamberlain, K.R., Tait, K.T., Schmitt, A.K., Darling, J.R., Barker, I.R., Hyde, B.C., 2013. Solving the Martian meteorite age conundrum using microbaddelevite and launch-generated zircon. Nature 499, 454–457.
- Parish, C.M., Field, K.G., Certain, A.G., Wharry, J.P., 2015. Application of STEM characterization for investigating radiation effects in BCC Fe-based alloys. J. Mater. Res. 30, 1275–1289.
- Perea, D.E., Arslan, I., Liu, J., Ristanovic, Z., Kovarik, L., Arey, B.W., Lercher, J.A., Bare, S.R., Weckhuysen, B.M., 2015. Determining the location and nearest neighbours of aluminium in zeolites with atom probe tomography. Nat. Commun. 6.
- Perea, D.E., Liu, J., Bartrand, J., Dicken, Q., Thevuthasan, S.T., Browning, N.D., Evans, J.E., 2016. Atom probe tomographic mapping directly reveals the atomic distribution of phosphorus in resin embedded ferritin. Sci. Rep. 6, 22321.
- Peterman, E.M., Reddy, S.M., Saxey, D.W., Snoeyenbos, D.R., Rickard, W.D.A., Fougerouse, D., Kylander-Clark, A.R.C., 2016. Nanogeochronology of discordant zircon measured by atom probe microscopy of Pb-enriched dislocation loops. Sci. Adv. 2, 1601318.
- Reddy, S.M., Saxey, D.W., Rickard, W.D.A., Fougerouse, D., Montalvo, S.D., Verberne, R., van Riessen, A., 2020. Atom probe tomography: development and application to the geosciences. Geostand. Geoanal. Res. 44, 5–50.
- Rickard, D., 2012. Sulfidic Sediments and Sedimentary Rocks. Elsevier.
- Rickard, 2019. How long does it take a pyrite framboid to form? Earth Planet. Sci. Lett. 513, 64–68.
- Rickard, 2021. Framboids. Oxford University Press.
- Sageman, B.B., Lyons, T.W., 2003. Geochemistry of fine-grained sedimentary rocks. In: Holland, H.D., Turekian, K.K. (Eds.), Treatise on Geochemistry. Pergamon, Oxford, pp. 115–158.
- Schreiber, D.K., Perea, D.E., Ryan, J.V., Evans, J.E., Vienna, J.D., 2018. A method for site-specific and cryogenic specimen fabrication of liquid/solid interfaces for atom probe tomography. Ultramicroscopy 194, 89–99.
- Stephenson, L.T., Moody, M.P., Liddicoat, P.V., Ringer, S.P., 2007. New techniques for the analysis of fine-scaled clustering phenomena within atom probe tomography (APT) data. Microsc. Microanal. 13, 448–463.
- Taylor, S.D., Liu, J., Arey, B.W., Schreiber, D.K., Perea, D.E., Rosso, K.M., 2018. Resolving iron(II) sorption and oxidative growth on hematite (001) using atom probe tomography. J. Phys. Chem. C 122, 3903–3914.
- Taylor, S.D., Liu, J., Zhang, X., Arey, B.W., Kovarik, L., Schreiber, D.K., Perea, D.E., Rosso, K.M., 2019. Visualizing the iron atom exchange front in the Fe(II)-catalyzed recrystallization of goethite by atom probe tomography. Proc. Natl. Acad. Sci. USA 116, 2866–2874.
- Thompson, K., Lawrence, D., Larson, D.J., Olson, J.D., Kelly, T.F., Gorman, B., 2007. In situ site-specific specimen preparation for atom probe tomography. Ultramicroscopy 107, 131–139.
- Valley, J.W., Cavosie, A.J., Ushikubo, T., Reinhard, D.A., Lawrence, D.F., Larson, D.J., Clifton, P.H., Kelly, T.F., Wilde, S.A., Moser, D.E., Spicuzza, M.J., 2014. Hadean age for a post-magma-ocean zircon confirmed by atom-probe tomography. Nat. Geosci. 7, 219–223.
- Viti, C., Frezzotti, M.-L., 2001. Transmission electron microscopy applied to fluid inclusion investigations. Lithos 55, 125-138.
- Vurpillot, F., Bostel, A., Blavette, D., 2000. Trajectory overlaps and local magnification in three-dimensional atom probe. Appl. Phys. Lett. 76, 3127–3129.
- White, L.F., Darling, J.R., Moser, D.E., Reinhard, D.A., Prosa, T.J., Bullen, D., Olson, D., Larson, D.J., Lawrence, D., Martin, I., 2017. Atomic-scale age resolution of planetary events. Nat. Commun. 8, 15597.
- Wilkin, R.T., Barnes, H.L., Brantley, S.L., 1996. The size distribution of framboidal pyrite in modern sediments: an indicator of redox conditions. Geochim. Cosmochim. Acta 60, 3897–3912.
- Wu, Y.-F., Fougerouse, D., Evans, K., Reddy, S.M., Saxey, D.W., Guagliardo, P., Li, J.-W., 2019. Gold, arsenic, and copper zoning in pyrite: a record of fluid chemistry and growth kinetics. Geology 47, 641–644.